Study on the Suitability of Numerical Integration at 5G Frequencies Using Unit Cube Test

Mario Cvetković, Dragan Poljak,
Ante Lojić Kapetanović
Faculty of Electrical Engineering, Mechanical
Engineering and Naval Architecture
University of Split, 21000 Split, Croatia
Email: [mcvetkov, dpoljak, alojic00]@fesb.hr

Hrvoje Dodig
Faculty of Maritime Studies
University of Split
21000 Split, Croatia
Email: hdodig@pfst.hr

***Abstract*—The assessment of human exposure to 5G mobile systems requires the use of numerical methods such as method of moments (MoM). MoM solution of the integral equation based formulation results in the fully populated system matrix whose filling time represents the most time-consuming operation for many problems. As the matrix size is directly related to the frequency of the problem, the numerical solutions in the 5G frequency range will thus put a tremendous computational cost both in terms of matrix fill time but also in the memory allocation. The paper is on the investigation of suitability of numerical integration at 5G frequencies using a unit cube test. The example of double surface integral in case of a combination of coplanar triangles is numerically solved using the Dunavant's symmetrical quadrature rules for triangles. The results show that depending on the discretization scheme, lower integration orders could be utilized, resulting in the reduced matrix fill time without actually sacrificing the accuracy.**

***Index Terms*—Dunavant rules; integral equation formulation; numerical integration; 5G frequencies; computational cost**

I. Introduction

The fifth generation (5G) of mobile communication systems is the significant evolution of the previous 4G LTE networks in terms of high transmission data rates, overall network capacity as well as a very low latency. 5G is expected to enable nearly instantaneous connectivity to billions of devices based on the use of millimeter waves operating in the GHz frequency range as well as beam steering technology by means of a massive multiple input, multiple output (MIMO) antenna systems.

The widespread use of the new MIMO systems having large number of elements will inevitably result in the public concern related to possible detrimental health effects. Compared to electromagnetic radiation in the radio frequency range, the thermal effects related to the mm-waves from the GHz part of the spectrum, are limited to the body surface due to small skin effect and low penetration depth. Nonetheless, in 2019 and 2020 IEEE standard [1] and ICNIRP guidelines [2], respectively, were revised in order to assure the compliance with the basic restrictions and consequently to ensure the safety of humans due to exposure to electromagnetic fields. Regardless of basic restriction quantity, defined by the specific absorption rate (SAR) in the range of up to 6 GHz, or the absorbed power density (APD) for frequencies above 6 GHz, the assessment of both quantities requires the use of sophisticated computational methods.

Recently, integral equation based methods resurfaced as one of the means for solving such problems [3], [4]. However, if the integral equation based formulations are used, the numerical solution accuracy will be influenced by the precision of calculated matrix system elements. Usually numerical integration is used to solve various double surface integrals, while taking into account the calculation speed as well as accuracy. In doing so, most often some compromise between the numerical efficiency and accuracy is required.

It is a well known fact that one of the drawbacks of using integral equation formulations is they result in a fully populated system matrix. The filling and the factoring (solving) of system matrix, are the two time-consuming operations required by MoM code with N unknowns [5]. In case of wire structures, these operations are of $O(N^2)$ for the former, and $O(N^3)$ for the latter, when direct solvers are used. However, in practice, matrix filling often requires more time spend. Since number of unknowns N is proportional to kd, with k and d being wave number and wire length, respectively, the asymptotic cost of these operations is of $O([kd]^3)$, clearly indicating the frequency scaling feature of the algorithm. Compared to wires, the asymptotic computational cost for surfaces is even more expensive, i.e. of $O([kd]^6)$, with matrix filling again dominating the computational runtime for most problems. On the other hand, the memory requirements for surfaces are of $O([kd]^4)$.

Another important thing to bear in mind is the size of the system matrix itself, as too large matrices becomes impossible to solve directly, e.g. using Gaussian elimination. Instead, an iterative procedure such as generalized minimum residual method (GMRES), [6], is required.

Recently, the graphics processing unit (GPU) has become another important resource regarding the computational capability compared to conventional central processing unit (CPU). The GPU has been used to speed up the conventional method of moments (MoM) calculations both in terms of filling time and splitting algorithm [7]. However, GPU computing requires additional effort as specialized adaptation of the code is necessary, e.g. rewriting in CUDA or other languages. Hence,

instead of immediate paradigm shift from CPU to GPU, we rather investigate how the application of a conventional MoM code could still be made more efficient without actually sacrificing accuracy, by the proficient use of the numerical integration rules.

This paper is on the investigation of numerical integration using a unit cube test. The organization of the paper is as follows: after introductory part, a brief description of the electric field integral equation (EFIE) formulation is given. The numerical solution of double surface integral latter used as a computational example is given, as well as brief descriptions of unit cube test and utilized quadrature rules for triangles. The results of several convergence tests, obtained at 5G frequencies are given in the next section, followed by the concluding remarks.

II. Mathematical Background

When using frequency domain surface integral equation (SIE) formulations, most often, the complex surface geometry of a problem is described using the triangular patches. This facilitates the use of a so called Rao-Wilton-Glisson (RWG) basis functions particularly developed for triangular patches [8].

A. Surface Integral Equation Formulation

This work is based on the frequency domain formulation for the homogeneous penetrable object. The electric field integral equation (EFIE) can be obtained using the equivalence theorem for the surface of the object and the appropriate boundary conditions (BC):

$$\left[-\vec{E}_n^{sca}(\vec{J},\vec{M})\right]_{tan} = \begin{cases} \left[\vec{E}^{inc}\right]_{tan}, & i=1 \\ 0, & i=2 \end{cases} \tag{1}$$

where E^{inc} is the known electric field impinging the scatterer and E^{sca} denotes the field scattered from the surface.

The tangential component of the electric field scattered from object surface can be written in terms of the equivalent surface electric and magnetic currents, $\vec{J}$ and $\vec{M}$, respectively, which can be expanded in terms of a linear combination of basis functions. Usually the so-called RWG basis functions [8] are used to expand $\vec{J}$, and orthogonal functions $\hat{n}\times$RWG are used to expand $\vec{M}$, as follows:

$$\vec{J}(\vec{r}) = \sum_{n=1}^{N} J_n \vec{f}_n(\vec{r}); \quad \vec{M}(\vec{r}) = \sum_{n=1}^{N} M_n \vec{g}_n(\vec{r}) \tag{2}$$

where J_n and M_n represent the coefficients to be determined, while N is the number of elements used to discretize the surface S of scatterer. As RWG functions are defined over a pair of triangles, the surface of scatterer needs to by meshed using a triangular patches.

SIE formulation of the problem via EFIE can be numerically solved e.g. using an efficient MoM scheme reported in [9]. Examples of application of a SIE based formulation include models of pediatric patients in e.g. transcranial magnetic stimulation (TMS) [10] or electromagnetic-thermal dosimetry [11], or even in a stochastic dosimetry of the human brain [12]. More details on the particular application can be found in [10]–[12].

Multiplying (1) by test functions $\vec{f}_m$, where $\vec{f}_m = \vec{f}_n$, and integrating over the scatterer surface S, followed by some additional steps [9], [13], yields the following system of linear integral equations

$$\sum_{n=1}^{N}\left(j\omega\mu_i A_{mn,i} + \frac{j}{\omega\varepsilon_i} B_{mn,i}\right) J_n + \\ + \sum_{n=1}^{N}\left(C_{mn,i} + D_{mn,i}\right) M_n = \begin{cases} V_m & , i=1 \\ 0 & , i=2 \end{cases} \tag{3}$$

where A_{mn}, B_{mn}, C_{mn}, and D_{mn} are related to various surface integrals, $i = 1, 2$ denote the regions outside and inside of the scatterer, respectively, while m and n are indices of source and observation triangles. Material properties of scatterer are taken into account via μ and ε, representing permeability and permittivity, respectively.

Integral equations set (3) can be written compactly in the matrix form as

$$[\mathbf{Z}] \cdot \{\mathbf{I}\} = \{\mathbf{V}\} \tag{4}$$

where size of system matrix $\mathbf{Z}$ is $2N \times 2N$, and size of source vector $\mathbf{V}$ is $2N$, as depicted on Fig. 1. It should be noted that thus formed system matrix $\mathbf{Z}$ is fully populated [4].

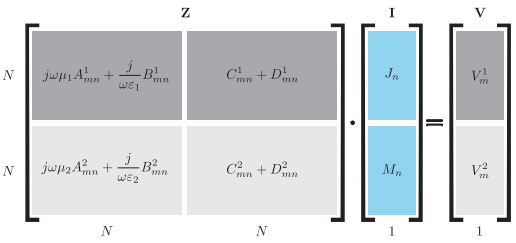

Fig. 1: The size of MoM system matrix [4]. Column vector $\mathbf{I}$ contains unknown coefficients used to determine equivalent surface electric and magnetic currents $\vec{J}$ and $\vec{M}$.

B. Numerical Integration of Double Surface Integrals

When determining elements of the system matrix, it is necessary to solve various surface integrals appearing in (3). One of the double surface integrals, whose numerical solution is considered in this work, is of the following form:

$$A_{mn} = \iint_S \vec{f}_m(\vec{r}) \cdot \iint_{S'} \vec{f}_n(\vec{r}\,') G(\vec{r},\vec{r}\,')\, dS'\, dS \tag{5}$$

where $\vec{f}_m$ is test function, and $\vec{f}_n = \vec{f}_m$ represents basis function expanded over triangles. Observation and source points are denoted by $\vec{r}$ and $\vec{r}\,'$, respectively. Rao-Wilton-Glisson (RWG) function is used as basis function [8]:

$$\vec{f}_n^{\pm}(\vec{r}) = \begin{cases} \dfrac{l_n}{2A_n^{\pm}}\vec{\rho}_n^{\pm} & ,\vec{r} \in T_n^{\pm} \\ 0 & ,\vec{r} \notin T_n^{\pm} \end{cases} \tag{6}$$

where l_n is the shared edge length at the interface between triangles T_n^+ and T_n^-, while A_n^+ and A_n^- denote the surface areas of triangles. Vector $\vec{\rho}_n^+ = \vec{r} - \vec{r}_n^+$ is directed from free vertex of T_n^+ while $\vec{\rho}_n^- = \vec{r}_n^- - \vec{r}$ is directed towards free vertex of T_n^-.

Integral (5) includes Green's function for the homogeneous medium given by:

$$G(\vec{r},\vec{r}\,') = \frac{e^{-jkR}}{4\pi R}; \quad R = |\vec{r} - \vec{r}\,'| \tag{7}$$

where R is the distance from observation to source point, while k is the wave number.

Depending on the distance between source and observation triangles, T_m and T_n respectively, particular approach to the solution of integral (5) is required. When observation and source triangles are far enough, numerical integration can be used. The numerical procedure (Gaussian quadrature) carried out in this work is related to evaluation of integral (5) in case of a coplanar source and observation triangles, numbered 1 and 2, as depicted on Fig. 2.

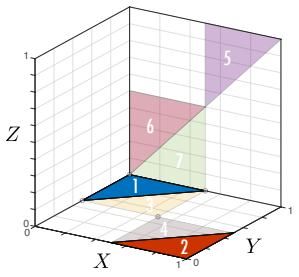

Fig. 2: Unit cube for testing various triangle combinations. Coplanar far triangles (numbered 1 and 2) considered as far combination in this study.

Inserting (6) and (7) into (5), the double surface integral can be written as

$$A_{mn} = \iint_S \frac{l_m}{2A_m^{\pm}}\vec{\rho}_m^{\pm}(\vec{r}) \cdot \iint_{S'} \frac{l_n}{2A_n^{\pm}}\vec{\rho}_n^{\pm}(\vec{r}\,')\frac{e^{-jkR}}{4\pi R}\,dS'\,dS \tag{8}$$

Each surface integral from (8) can be approximated by a weighted coefficients sum. On a triangular domain, this approximation can be written as:

$$\iint_T f(\alpha,\beta,\gamma)\,dS \approx A\sum_{i=1}^{N} w_i(\alpha_i,\beta_i,\gamma_i) f(\alpha_i,\beta_i,\gamma_i) \tag{9}$$

where A is triangle area, $w_i(\alpha_i,\beta_i,\gamma_i)$ are weighting coefficients normalized to triangle area, while α_i, β_i, and γ_i are local or simplex coordinates (defined on unit triangle).

Utilizing (9) in (8), results in

$$A_{mn} = \frac{l_m l_n}{16\pi A_m^{\pm} A_n^{\pm}} A_m^{\pm} \sum_{p=1}^{M} w_p \vec{\rho}_m^{\pm}(\vec{r}_p) \cdot \cdot A_n^{\pm} \sum_{q=1}^{N} w_q \vec{\rho}_n^{\pm}(\vec{r}\,'_q)\frac{e^{-jkR_{pq}}}{R_{pq}} \tag{10}$$

and after some cancellation and rearranging, the following expression is obtained:

$$A_{mn} = \frac{l_m l_n}{16\pi}\sum_{p=1}^{M}\sum_{q=1}^{N} w_p w_q \vec{\rho}_m^{\pm}(\vec{r}_p) \cdot \vec{\rho}_n^{\pm}(\vec{r}\,'_q)\frac{e^{-jkR_{pq}}}{R_{pq}} \tag{11}$$

with $R_{pq} = |\vec{r}_p - \vec{r}\,'_q|$, where $\vec{r}_p$, $\vec{r}\,'_q$, w_p and w_q denote the location of Gaussian points and weights for the source and observation triangles, respectively. M and N, represent the number of integration points for the source and observation triangle, respectively, dependent on the order of integration, $P = 1,\ldots,20$, and $Q = 1,\ldots,20$.

C. Dunavant's Quadrature Rules for Triangles

Dunavant's symmetric quadrature rules for triangles are used in this work. The quadrature rules of degree up to $P = 20$, with associated quadrature points and weighting coefficients can be found in [14].

While there are many other rules available [15]–[19], Dunavant's rules are nowadays most frequently used integration rules for triangles, and similar to classical Gaussian quadratures, an n-point rule is exact for all polynomials of orders up to $2n-1$, [18]. Although some of the rules have undesirable features such as nodes position outside the triangle and negative weights, Dunavant's rules are optimal in the sense that for a given rule, the number of nodes used is close to or even theoretically equal to the smallest possible value [20], which makes them highly efficient for problems requiring solutions to a large number of integrals. Furthermore, these rules use the symmetrical position of the integration nodes with respect to the vertices of the triangles, thus eliminating possible variations in the order in which they are assigned [20].

Using a various combinations of integration orders $P = 1,\ldots,20$ and $Q = 1,\ldots,20$, for the source and the observation triangles, the double surface integral (5) is solved using expression (11).

D. Unit Cube Test

The unit cube test, depicted on Fig. 2, utilized for testing the interaction between source and observation triangles, was introduced in [21]. The unit cube is meshed with 48 triangular patches, with 8 isosceles triangles on each cube side. Utilizing the cubical shape, various combinations of coplanar and orthogonal triangles could be tested. Furthermore, the unit cube and the associated mesh can be easily scaled to enable testing at various frequencies of interest.

Figure 3 illustrates the comparison of triangular element size when unit cube scale is halved in several iteration steps ($n =$

$1, \ldots, 8$). The discretization steps numbered $n = 4, 5, 6, 7, 8$ are latter denoted as: $1/8$, $1/16$, $1/32$, $1/64$, and $1/128$, discretization schemes, respectively.

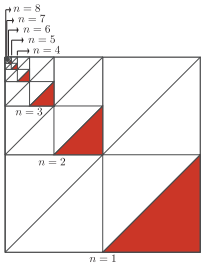

Fig. 3: Illustration of triangular element size on one side of unit qube, depending on the scaling iteration number $n = 1, \ldots, 8$.

III. Results

Utilizing the unit cube test, the following results are obtained. All reported results are related to numerical solution of double surface integral (5) in case of a far triangle interaction. The numerical solutions are obtained using various (P,Q) combination of integration orders for source and observation triangles, with $P = 1, \ldots, 20$ and $Q = 1, \ldots, 20$.

The first set of results, shown on Fig. 4, are obtained at several 5G frequencies currently utilized or to be used in Croatia (0.7 GHz, 3.6 GHz, 26 GHz, 90 GHz), as well as 6 GHz, considered as the transition frequency related to basic restriction quantities [3].

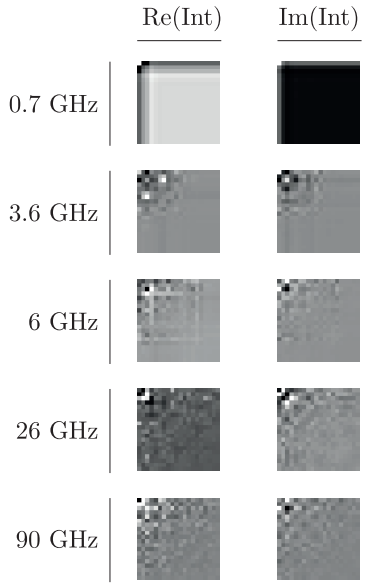

Fig. 4: Effect of increasing frequency. Convergence of real and imaginary part of integral A_{mn} with increasing frequency. Source and observation triangles (1 and 2) sharing no points (far term).

As seen from Fig. 4, the convergence of real and imaginary parts of integral A_{mn} are depicted on (P,Q) square, with respect to utilized frequency. The grey colour shade of (P, Q) square, represents the value of integral obtained using P and Q orders of integration for both triangles, where the increase of integration order is from left to right for Q, and from top to bottom for P.

At 0.7 GHz, it is evident that increase of integration points, results in the convergence on the real and imaginary part of the solution. When interpreting the (P, Q) square, it should be bared in mind that the gray colour itself is not essential. Instead, the colour of the complete square is. As example at 0.7 GHz clearly shows, going from top left to bottom right, the shade of grey becomes uniform, meaning that the solution converges. On the other hand, checkered patterns, which occur at other considered frequencies, suggest that higher integration orders are required (at 3.6 GHz and 6 GHz), but also that convergence can not be guaranteed (at 26 GHz and 90 GHz) and further steps are in order (such as finer discretization).

The following set of results, shown on Fig. 5, depict the convergence with respect to various discretization schemes of unit cube: $1/8$, $1/16$, $1/32$, $1/64$, and $1/128$. All the results are represented as relative error with respect to reference value according to:

$$\text{Relative error} = \frac{|I_{\text{quadrature}} - I_{\text{reference}}|}{|I_{\text{reference}}|} \tag{12}$$

where $I_{\text{quadrature}}$ denotes the value at particular quadrature order (P,Q), while $I_{\text{reference}}$ is the reference value selected as the highest integration order, i.e. $P = 20, Q = 20$.

It can be clearly seen from Fig. 5 that finer discretization ($1/32$, $1/64$, $1/128$) results in rather similar convergence rate regardless of the frequency. Compared to that, coarser discretizaton ($1/8$, $1/16$), i.e. larger size of triangular elements, results in rather low convergence rate. This is particularly pronounced at higher frequencies, where coarser discretization schemes result in rather large relative error, even at highest utilized integration orders. Hence, the results show that, depending on the required accuracy, i.e. relative error, at higher frequencies the only option is to utilize finer discretization resulting in larger number of triangular elements, and consequently, larger system matrix.

However, as already mentioned, finer discretization raises the computational requirements, related to both matrix filling time as well as matrix storage. Related to latter, Fig. 6 shows the number of matrix elements and related matrix size in GB, when double precision is used.

Table I compare the matrix size and memory allocation in case of a unit cube scaled using several iteration steps n, $n = 1, \ldots, 8$.

Table I shows that as the number of elements is increased, the memory allocation becomes significant burden at finest discretizations ($1/64$, $1/128$), while even relatively coarse discretizations such as $1/16$ and $1/32$ result in matrix size where iterative solution procedures such as GMRES should be considered.

Another important thing to consider is the time required to fill the system matrix, which is directly related to number of elements as well as a number of operations, again related

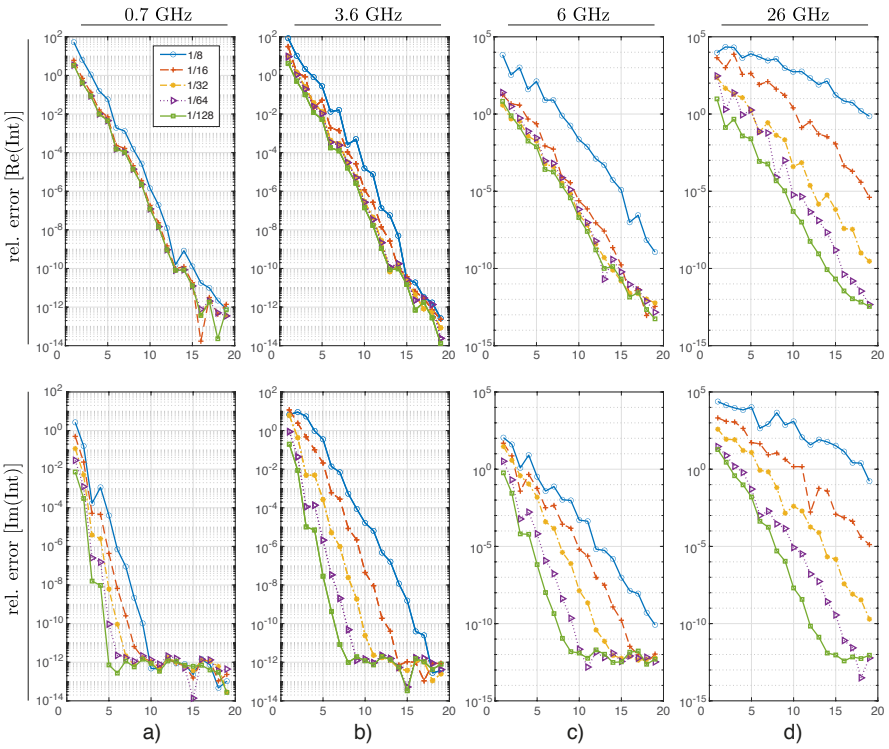

Fig. 5: Convergence of the real part (1st row) and imaginary part (2nd row) of the solution wrt. $P = 20, Q = 20$ integration rule, using several discretization schemes ($1/8$, $1/16$, $1/32$, $1/64$, $1/128$) at: a) 0.7 GHz, b) 3.6 GHz, c) 6 GHz, d) 26 GHz. All x-axes denote $P = Q = 1 \ldots 20$.

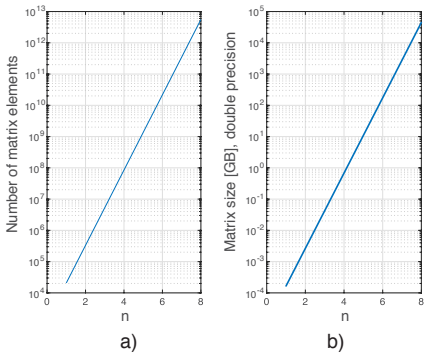

Fig. 6: a) Number of system matrix elements and b) resulting memory allocation in GB using the double precision, depending on the scaling iteration number $n = 1, \ldots, 8$.

TABLE I: Parameters of unit cube and related number of elements: n - scaling iteration; k - scaling factor; T - triangles per unit cube side; L - number of specific triangle interactions per cube side; N - total number of RWG elements (for cube); N_Z - number of elements of system matrix; Memory allocation for system matrix.

	k	$T = 2^{2n+1}$	$L = [n\cdot(n-1)+1]^2$	$N = 6T\cdot 3/2$	$N_Z = (2N)^2$	Memory
$n = 1$	$1/1$	8	1	72	20.736	165 KB
$n = 2$	$1/2$	32	9	288	331.776	2,65 MB
$n = 3$	$1/4$	128	49	1152	5.308.416	42,4 MB
$n = 4$	$1/8$	512	169	4608	84.934.656	679,5 MB
$n = 5$	$1/16$	2048	441	18.432	1.35 E09	10,87 GB
$n = 6$	$1/32$	8192	961	73.728	2.17 E10	173,9 GB
$n = 7$	$1/64$	32.768	1849	294.912	3.47 E11	2,78 TB
$n = 8$	$1/128$	131.072	3249	1.179.648	5.56 E12	44,53 TB

to integration order. Fig. 7 shows the normalized CPU time dependent on the combination of integration orders P and Q.

As seen from Fig. 7, obtained as an average value of 10.000 runs for each (P,Q) combination, selecting lower integration orders, even with modest number of integration points, the computational time can be reduced in half. Again, the decision for this will depend on the required calculation precision.

Finally, the question as to which integration order to select should be addressed. This can be illustrated in the following way, as showed on Fig. 8, where each field from the square denotes the total number of integration points used on both triangles. Examples of several integration orders, namely $(P, Q) = (7, 7), (8, 8), (9, 9), (10, 10)$, and $(11, 11)$, are compared with lower integration orders at several discretization schemes ($1/8$ - green, $1/16$ - purple, $1/32$ - red, $1/64$ - blue, $1/128$ - yellow). All the coloured fields denote the integration order with lower relative error compared to considered $P = Q$ order. All the coloured fields obtained using finer discretization schemes include also the fields from coarser discretization.

For example, consider situation on Fig. 8a), where $(P, Q) = (7, 7)$ includes 26 integration points. Compared to this, at

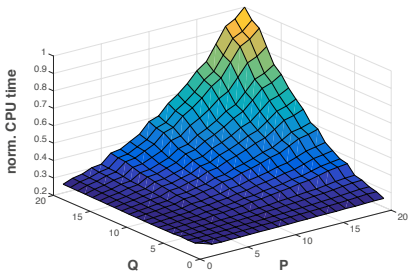

Fig. 7: Normalized CPU time wrt. $P = 20, Q = 20$ integration rule. Value for each P,Q combination obtained as an averaged time of 10.000 runs.

discretization level $1/32$, all the red and purple coloured fields denote integration orders with higher precision. These results suggest that, depending on the discretization scheme, lower integration order could be utilized, therefore, reducing the matrix filling time without actually sacrificing the solution accuracy.

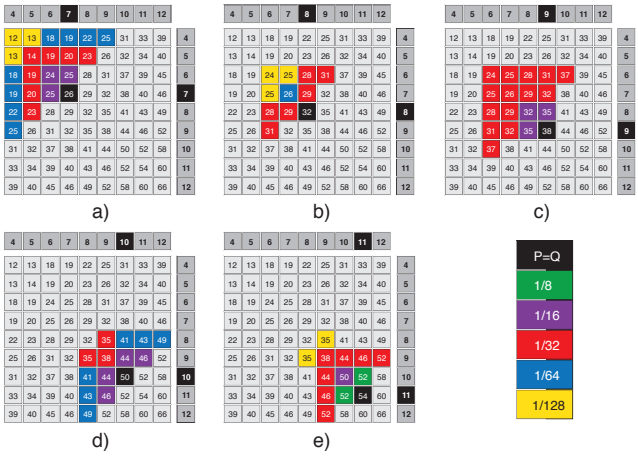

Fig. 8: Application of lower integration order resulting in higher precision. Example of integration order: a) $(P, Q) = (7, 7)$, b) $(P, Q) = (8, 8)$, c) $(P, Q) = (9, 9)$, d) $(P, Q) = (10, 10)$, e) $(P, Q) = (11, 11)$. The first row and last column denote the integration order.

IV. Conclusion

This paper investigated the suitability of numerical integration of double surface integral on a pair of coplanar triangles using a unit cube test. Several examples are considered at frequencies related to 5G system. The results show that solution at frequencies from the higher GHz range require the use of higher quadrature orders as well as finer discretization schemes, resulting in significantly increased requirements for matrix storage as well as matrix fill time. On the other hand, at lower GHz range, results suggest that utilizing the Dunavant's quadrature rules for triangles, depending on the discretization scheme, lower integration orders could be used, thereby facilitating the decrease of matrix fill time without actually lowering the accuracy of the solution. Further investigation should be carried out to examine if this reduction in the computational requirements could be facilitated in case of other triangle combinations.

References

[1] IEEE, "IEEE Standard for safety levels with respect to human exposure to electric, magnetic, and electromagnetic fields, 0 Hz to 300 GHz," *IEEE Std C95.1-2019 (Revision of IEEE Std C95.1-2005)*, pp. 1–312, 2019.

[2] ICNIRP, "Guidelines for limiting exposure to electromagnetic fields (100 kHz to 300 GHz)," *Health Physics*, vol. 118, no. 5, pp. 483–524, 2020.

[3] A. Šušnjara, H. Dodig, D. Poljak, and M. Cvetković, "Stochastic-deterministic thermal dosimetry below 6 GHz for 5G mobile communication systems," IEEE Transactions on Electromagnetic Compatibility, accepted for publication.

[4] D. Poljak and M. Cvetković, *Human Interaction with Electromagnetic Fields: Computational Models in Dosimetry*. Academic Press, 2019.

[5] D. B. Davidson, *Computational electromagnetics for RF and microwave engineering*. Cambridge University Press, 2010.

[6] Y. Saad and M. H. Schultz, "Gmres: A generalized minimal residual algorithm for solving nonsymmetric linear systems," *SIAM Journal on scientific and statistical computing*, vol. 7, no. 3, pp. 856–869, 1986.

[7] S. Peng and Z. Nie, "Acceleration of the method of moments calculations by using graphics processing units," *IEEE Transactions on Antennas and Propagation*, vol. 56, no. 7, pp. 2130–2133, 2008.

[8] S. Rao, D. R. Wilton, and A. Glisson, "Electromagnetic scattering by surfaces of arbitrary shape," *IEEE Transactions on Antennas and Propagation*, vol. 30, no. 3, pp. 409–418, May 1982.

[9] M. Cvetković and D. Poljak, "An efficient integral equation based dosimetry model of the human brain," in *Proceedings of 2014 International Symposium on Electromagnetic Compatibility (EMC EUROPE) 2014, Gothenburg, Sweden, 1-4 September 2014*, 2014, pp. 375–380.

[10] M. Cvetković, D. Poljak, M. Rogić Vidaković, and Z. Dogaš, "Transcranial magnetic stimulation induced fields in different brain models," *Journal of Electromagnetic Waves and Applications*, vol. 30, no. 14, pp. 1820–1835, 2016.

[11] M. Cvetković and D. Poljak, "Electromagnetic-thermal dosimetry comparison of the homogeneous adult and child brain models based on the SIE approach," *Journal of Electromagnetic Waves and Applications*, vol. 29, no. 17, pp. 2365–2379, 2015.

[12] M. Cvetković, S. Lallechere, K. E. Khamlichi Drissi, P. Bonnet, and D. Poljak, "Stochastic sensitivity in homogeneous electromagnetic-thermal dosimetry model of human brain." *Applied Computational Electromagnetics Society Journal*, vol. 31, no. 6, 2016.

[13] M. Cvetković, D. Poljak, and J. Haueisen, "Analysis of transcranial magnetic stimulation based on the surface integral equation formulation," *Biomedical Engineering, IEEE Transactions on*, vol. 62, no. 6, pp. 1535–1545, June 2015.

[14] D. A. Dunavant, "High degree efficient symmetrical gaussian quadrature rules for the triangle," *International Journal for Numerical Methods in Engineering*, vol. 21, no. 6, pp. 1129–1148, 1985.

[15] P. C. Hammer, O. J. Marlowe, and A. H. Stroud, "Numerical integration over simplexes and cones," *Mathematical Tables and Other Aids to Computation*, vol. 10, no. 55, pp. 130–137, 1956.

[16] P. Silvester, "Symmetric quadrature formulae for simplexes," *Mathematics of Computation*, vol. 24, no. 109, pp. 95–100, 1970.

[17] G. R. Cowper, "Gaussian quadrature formulas for triangles," *International Journal for Numerical Methods in Engineering*, vol. 7, no. 3, pp. 405–408, 1973.

[18] S. Wandzura and H. Xiao, "Symmetric quadrature rules on a triangle," *Computers and Mathematics with Applications*, vol. 45, no. 12, pp. 1829–1840, 2003.

[19] L. Zhang, T. Cui, and H. Liu, "A set of symmetric quadrature rules on triangles and tetrahedra," *Journal of Computational Mathematics*, vol. 27, no. 1, pp. 89–96, 2009.

[20] J. S. Savage and A. F. Peterson, "Quadrature rules for numerical integration over triangles and tetrahedra," *IEEE Antennas and Propagation Magazine*, vol. 38, no. 3, pp. 100–102, 1996.

[21] M. Cvetković, D. Poljak, A. Lojić Kapetanović, and H. Dodig, "Unit cube test for double surface integrals in frequency domain integral equation formulations," submitted to 5th International Conference on Smart and Sustainable Technologies (SpliTech 2021).